

# Characterization of defect structures in nanocrystalline materials by X-ray line profile analysis

Jenő Gubicza and Tamás Ungár\*

Department of Materials Physics, Institute of Physics, Eötvös Lorand University, P.O. Box 32, 1518 Budapest, Hungary

Received April 14, 2007; accepted August 30, 2007

*X-ray line profile analysis / Nanomaterials / Crystallite size / Dislocations / Planar defects*

**Abstract.** X-ray line profile analysis is a powerful alternative tool for determining dislocation densities, dislocation type, crystallite and subgrain size and size-distributions, and planar defects, especially the frequency of twin boundaries and stacking faults. The method is especially useful in the case of submicron grain size or nanocrystalline materials, where X-ray line broadening is a well pronounced effect, and the observation of defects with very large density is often not easy by transmission electron microscopy. The fundamentals of X-ray line broadening are summarized in terms of the different qualitative breadth methods, and the more sophisticated and more quantitative whole pattern fitting procedures. The efficiency and practical use of X-ray line profile analysis is shown by discussing its applications to metallic, ceramic, diamond-like and polymer nanomaterials.

## 1. Introduction

The physical, chemical and mechanical properties of nanocrystalline materials are basically influenced by their defect structure. X-ray line profile analysis (LPA) has been proved to be a powerful method for characterising the defect structure in submicron grain size or nanocrystalline materials. Electron microscopy is probably one of the most direct methods to determine the character and spatial distribution of crystal defects, however, the X-ray method, on the one hand, is non-destructive, and on the other hand, it provides average values with better statistics of the different parameters of the defect structure. The two different methods are in some sense alternative and complementary to each other. For example, the dislocation density can only be determined by LPA if it is larger than about  $5 \times 10^{12} \text{ m}^{-2}$ , while transmission electron microscopy (TEM) can only be used if the local dislocation density is smaller than about  $5 \times 10^{14} \text{ m}^{-2}$ . In the case of X-ray diffraction, at dislocation densities smaller than  $5 \times 10^{12} \text{ m}^{-2}$  the breadths of physical diffraction peaks become identical

to the corresponding Darwin breadths, whereas in the case of TEM, at dislocation densities larger than  $5 \times 10^{14} \text{ m}^{-2}$  the contrasts of individual dislocations start overlapping. Weak beam techniques can extend the range somewhat further, but  $10^{15} \text{ m}^{-2}$  local dislocation density is probably the absolute upper limit where individual dislocations can be distinguished in a TEM micrograph. In the case of heterogeneous dislocation distributions the  $10^{15} \text{ m}^{-2}$  local density values can correspond to  $10^{13} \text{ m}^{-2}$  or  $5 \times 10^{13} \text{ m}^{-2}$  average density values which are typically low dislocation densities in the case of plastically deformed materials, and especially low values in the case nanocrystalline materials.

LPA and TEM are not only alternative methods, but they provide different aspects of the microstructure. For example, though both, electrons and X-rays obey Bragg's law, since their interaction with matter is so different they reveal different features of the microstructure of materials, especially nanomaterials. X-rays interact weakly with matter and penetrate deep from a few  $\mu\text{m}$  to millimeters, whereas electrons interact strongly, transmitting only 10 to 100 nanometers. The extinction length of X-rays is about two to three orders of magnitude longer than that of electrons. This explains why X-rays are sensitive to long-range features, average crystal structures, and average deviations from long-range order, especially lattice strains and stresses. While electrons are able to reveal the most local atomic structure in TEM down to individual lattice sites, they are unable to reveal long-range strain fields. In that sense the concomitant application of LPA and different electron microscopic methods, e.g. TEM and scanning electron microscopy (SEM), or electron back scattering diffraction (EBSD) provide certainly the best complex microstructure and defect characterisation in nanocrystalline materials. The main defect types or microstructural properties of which LPA can provide information are the (i) average crystallite size and (ii) size distribution, cf. [1–20], (iii) average dislocation density and (iv) dislocation character, cf. [21–32] (v) slip activity, (vi) active Burgers vectors, cf. [27, 28, 33–36], and (vii) planar defect densities, cf. [1, 2, 29, 37–51] or (viii) different types of internal stresses of first and second order, (ix) especially long-range-internal stresses prevailing in heterogeneous microstructures, cf. [52–58], (x) fluctuation of chemical composition, cf. [59], (xi) anti-phase boundaries, cf. [60, 61] or point defects, especially vacancy concentrations, cf. [62].

\* Correspondence author (e-mail: ungar@ludens.elte.hu)

One of the important advantages of using TEM is that it gives a direct image of the microstructure. Contrary to this, the method of LPA reflects indirect information about the microstructure of materials. This means that the interpretation of LPA results needs modeling of the microstructure. For the construction and control of realistic models, almost permanent and simultaneous TEM investigations are necessary. On the other hand, it has to be mentioned that the statistics of the quantities determined by LPA is much better than that of TEM, since the sampling of materials or volumes by X-ray diffraction is about  $10^7$  to  $10^9$  larger than by a TEM micrograph. In the case of nanomaterials this means that, while a TEM micrograph sees 10 to 100 nanograins, an X-ray diffraction pattern is usually obtained from  $10^8$  to  $10^{10}$  nanograins or crystallites. A further technical aspect may also be mentioned, that the sample preparation for TEM, especially in the case of nanomaterials, is often time consuming and needs special devices, *e.g.* ion beam milling, compared to qualitatively simpler specimen preparation for the purpose of X-ray diffraction experiments.

Nanocrystalline materials can either be in the form of loose powders or compact bulk materials, ceramics, ionic crystals or metals and they can be produced by different methods, like inert gas condensation and compaction, ball milling, thermal plasma synthesis, or chemical methods using precursors, or severe plastic deformation, or crystallized from the bulk amorphous state. LPA has the great advantage that it can be applied for all different types of materials irrespective of synthesis or constitution. The possible types of defects in nanocrystalline materials are believed to be the same as for microcrystalline materials, therefore the methods applied in the evaluation of line broadening of nanomaterials are the same as used for large-grained specimens. The density of defects and their influence on physical and mechanical properties of nanomaterials are expected to be different from coarse-grained counterparts.

Cervellino [63] has shown that when the crystallite size becomes smaller than about 5 nm the peak intensities of Bragg reflections are changed by a few percent. This effect is caused by the interference of waves scattered by different particles, especially when there is absolutely no texture, not even a local texture. Other authors have shown that when the nanocrystalline specimen is textured [14] or when in a nano-powder specimen the adjacent crystallites are locally textured [64], the profiles of Bragg reflections closest to the origin of reciprocal space can become considerably narrower than what would correspond to the true coherence length of the particles. This latter is the consequence of a specific X-ray optical interference effect causing unusual peak narrowing in the first few Bragg reflections in powder patterns.

The defect and microstructure can be characterized by the following fundamental features: (a) the grain or crystallite size, (b) lattice defects producing microstrain whose effect can be summarized in the mean square strain:  $\langle \varepsilon^2 \rangle$ , (c) planar defects, especially stacking faults and twin boundaries. Due to the high fraction of grain boundaries in nanomaterials, grain boundaries and relaxed surface-near regions are a further defect type present in these ma-

terials. This defect type and its effects on diffraction is the topic of another paper in the present special issue [65] and will not be treated here.

It is noted here that, a review on LPA has recently been published in the same journal by the same authors [66]. It is important, however, that authors have taken special care to avoid overlap of the subject matter of [66] and the present paper. Moreover, the present review deals with the effects of planar defects and polymers which were not treated in [66]. Finally, the method of LPA developed to such an extent during the last decades that it is hard to review in detail the whole field in a single journal paper.

## 2. Fundamentals of X-ray line profile analysis

In nanocrystalline materials X-ray diffraction profiles broaden due to three different lattice defect types: (i) small crystallite size, (ii) dislocations or dislocation type defects and (iii) planar defects, especially stacking faults and twin boundaries. The X-ray line broadening effects produced by these three major defect types have distinctively different and well defined *hkl* dependence, which is the physical basis for separating them from each other. It can be shown that well defined profile functions can be attributed to the three major defect types, *i.e.* the *size profile*,  $I^S$  to (i) small crystallite size [15, 30, 67–69], the *strain profile*,  $I^D$  to (ii) dislocations or dislocation type defects [21–23, 27, 30, 32, 52, 53] and the *stacking fault profile*,  $I^{SF}$  to (iii) planar defects [42–44, 51]. In the presence of all these defect types, the physical profile,  $I^{PHYS}$  is the convolution of these three profile functions [1]:

$$I^{PHYS} = I^S \times I^D \times I^{SF}. \quad (1)$$

One of the main tasks of the theory of LPA is to produce adequate microstructural models for the individual profile functions. A brief summary of current models for the three profile functions in Eq. (1) is given in paragraphs 2.2 and 2.3 below.

### 2.1 Modified Williamson-Hall plot and modified Warren-Averbach method

Size broadening is fundamentally diffraction order independent [1, 67, 69]. It may have an *hkl* dependence, especially if the crystallite shape is considerably deviating from being globular or spherical, *cf.* [62, 69–72]. Strain broadening, on the other hand is increasing with diffraction order [1, 73]. This global difference in the order dependence, or in other words *hkl* dependence, is the basis for the two classical methods of X-ray line profile analysis: (a) the Williamson-Hall plot [73] and (b) the Warren-Averbach method [1]. None of these methods, however, takes into account strain anisotropy. Especially, in the Warren-Averbach procedure it was voluntarily suggested [1] to overcome this problem by restricting the analysis to series of harmonic reflections. Strain anisotropy means that neither the full width at half maximum (FWHM) nor the integral breadths ( $\beta$ ) in a Williamson-Hall plot, nor the Fourier coefficients in the Warren-Averbach plot are monotonous functions of  $\sin \theta$  or  $(\sin \theta)^2$ , respectively. In

plastically deformed metals the effect was first observed in the early forties by Stokes and Wilson [74], which, however, did not attract much attention until the eighties. Kuzel and Klimanek [75, 76] and Ungár *et al.* [77, 78] have realized that strain anisotropy can be used to characterize the dislocation structure in more detail. In the *modified* Williamson-Hall plot [68, 77] the FWHM or the integral breadths,  $\Delta K_{\text{FWHM}}$  or  $\Delta K_{\beta}$ , are scaled versus  $K^2\bar{C}$ , where  $K = 2 \sin \theta/\lambda$ ,  $\theta$  is the diffraction angle and  $\lambda$  is the wavelength of X-rays and  $\bar{C}$  is the average dislocation contrast factor, cf. [31, 68]:

$$\Delta K_{\text{FWHM},\beta} = 1/d + \alpha K^2\bar{C} + O(K^2\bar{C})^2, \quad (2)$$

where  $d$  is an apparent crystallite size,  $\alpha$  is a constant and  $O$  stands for higher order terms in  $K^2\bar{C}$ . For spherical crystallites the volume weighted diameter  $\langle x \rangle_{\text{vol}}$  is directly related to  $d$ :  $\langle x \rangle_{\text{vol}} = (4/3)d$  [79]. In the *modified* Warren-Averbach method [68, 77] the Fourier coefficients are scaled versus  $K^2\bar{C}$  and the mean square strain is explicitly given for dislocations:

$$\ln A(L) \cong \ln A^S(L) - (\varrho\pi b^2/2) L^2 \ln(R_e/L) (K^2\bar{C}), \quad (3)$$

where  $A(L)$  and  $A^S(L)$  are the Fourier coefficients of the *physical* and the *size* profiles, respectively,  $\varrho$  is the average dislocation density,  $L$  is the Fourier variable and  $R_e$  the effective outer cut-off radius of dislocations. The value of  $R_e$  characterizes the arrangement of dislocations which is also an important feature of dislocation structure beside the density. Though strain anisotropy is appropriately taken into account in the *modified* Williamson-Hall plot, since strain is only appearing in the slope,  $\alpha$ , the two parameters necessary to describe the dislocation structure, *i.e.*  $\varrho$  and  $R_e$ , cannot be determined separately. In the *modified* Warren-Averbach method, however, since both,  $\varrho$  and  $R_e$ , appear separately, the procedure can provide the two parameters simultaneously, cf. [30].

The method of *modified* Williamson-Hall plot [68, 77] is not an exact method in the sense that the breadths corresponding to size or strain contribute in different ways depending on the specific profile functions of the two effects. Especially, in the two cases when both profile functions are either Gaussian or Lorentzian, the breadths add up in quadratic or linear manner, respectively. In reality the profile functions are never clear Gaussian or Lorentzian, especially in the case of strain profiles [27, 80]. In spite of that the *modified* Williamson-Hall plot can provide extremely valuable information about the qualitative nature of line broadening, cf. [34, 75, 76, 81, 82]. The *modified* Warren-Averbach method [68, 77], on the other hand is physically exact, with the only constraint that it works with the smaller values of the Fourier variable. In diffraction or reciprocal space this means that it works with the tail part of the diffraction maxima, more specifically, with the intensities below about half the maxima. In fact, this method provides the physical basis for the strain profile in all the whole profile or whole pattern methods developed by different groups, cf. [30, 32, 68, 83–85]. The central part of the strain profile is described by the Wilkens function [22, 23] which, however, is still topic of discussion, cf. [27].

## 2.2 Whole profile and whole patterns methods

Whole profile methods, though more laborious, provide more reliable and more refined microstructure data than either the breadth methods or the *modified* Warren-Averbach method. The philosophy of whole profile or whole pattern methods is that the different microstructure features, *i.e.* size, strain or faulting can be described by uniform profile functions, and that the *hkl* dependence of these uniform profile functions can be given by appropriate scaling rules in a relatively simple manner. The uniform size profile is the squared Fourier transform of the form-factor of a crystallite in the direction of the diffraction vector modulated by an appropriate size-distribution-density function. Assuming log-normal size distribution the size profile can be written as [65, 83, 85]:

$$I^S(s) = \int_0^{\infty} t \frac{\sin^2(t\pi s)}{(\pi s)^2} \operatorname{erfc} \left[ \frac{\ln(t/m)}{\sqrt{2}\sigma} \right] dt, \quad (4)$$

where  $s = (2 \cos \theta/\lambda) \Delta\theta$ ,  $\operatorname{erfc}$  is the complementary error function, and  $m$  and  $\sigma$  are the median and variance of the log-normal size-distribution density function defined as:

$$f(x) = \frac{1}{\sqrt{2\pi}\sigma} \frac{1}{x} \exp \left[ -\frac{[\ln(x/m)]^2}{2\sigma^2} \right]. \quad (5)$$

With  $m$  and  $\sigma$  the arithmetic-, the area- and the volume-weighted mean crystallite diameters are [79]:

$$\langle x \rangle_j = m \exp(k\sigma^2) \quad (6)$$

where  $k = 0.5, 2.5$  and  $3.5$  in the case of arithmetic-, area- and volume-weighted mean and  $j$  stands for these different averages, respectively.

The strain profile is given through its Fourier coefficients [22, 23]:

$$A^D(L) = \exp \{ -2\pi^2 L^2 K^2 \langle \varepsilon_{g,L^2} \rangle \}, \quad (7)$$

where the mean square strain in dislocated crystals can be given by the Wilkens function  $f(\eta)$  [23]:

$$\langle \varepsilon_{g,L^2} \rangle \cong \frac{\varrho C b^2}{4\pi} f(\eta), \quad (8)$$

and  $\eta = L/R_e$ . In a polycrystal, or if all possible slip systems are equally populated the dislocation contrast factors can be averaged over the permutations of the *hkl* indices and the mean square strain is [31, 84]:

$$\langle \varepsilon_{g,L^2} \rangle \cong \frac{\overline{\varrho C b^2}}{4\pi} f(\eta). \quad (9)$$

The averaging can be constrained over only the contrast factors if only a single Burgers vector is conceivable in the crystal. If, however, more Burgers vectors can be present, especially with different absolute values, as *e.g.* in hexagonal, orthorhombic or tetragonal crystals, the averaging has to be extended over the Burgers vectors, as indicated by the bar in Eq. (9).

## 2.3 Incorporation of planar defects

In crystals with planar faults the determination of uniform profile functions has recently been done for *fcc* [51, 85,

86] and hexagonal crystals [88, 89]. There are three types of planar faults: intrinsic, extrinsic stacking faults and twins. Stacking faults or twin boundaries have two different effects in diffraction: (1) they cause a phase shift which breaks down coherent scattering, and (2) since they are planar defects, they may cause homogeneous deformations, cf. [21, 90]. Latter means change in lattice constant which appears as line shifts. Assuming that each crystallite or grain contains only one type of planar defect, *i.e.* either twin boundaries on a specific lattice plane or stacking faults also on specific lattice planes, line broadening and line shifts pertain to specific selection rules of  $hkl$  indices within the  $hkl$  family of lattice planes. This is illustrated in Fig. 1, where profiles of the {422} Bragg reflection (solid line) and sub-reflections (dash, dash-dot, and dotted lines, respectively) corresponding to various  $hkl$  conditions for 10% intrinsic stacking faults, calculated in [51] by the DIFFaX [42] software are shown. The dotted line corresponds to an unaffected, delta-function like sub-reflection where the  $hkl$  condition is:  $h + k + l = \pm 3n$  (with  $n = 0, 1, 2, \dots$ ). The other two sub-reflections correspond to  $h + k + l = \pm 8$  and  $h + k + l = \pm 4$ , and are shifted in opposite directions, and have different broadening. The resultant profile (solid line) is asymmetrically broadened and has a delta function like component. In [51, 88, 89] it was shown that the sub-reflections, apart from the delta-function like components, are Lorentzian functions as far as  $10^{-4}$  relative intensities down into their tails. In [51] it was shown that peak broadening caused by faulting does not increase with diffraction order. This suggests that line broadening caused by faulting or twinning is of *size* type. It is, however, a complicated *size* type line broadening, since the sub-reflections are shifted in different manner according to specific  $hkl$  selection rules, cf. [37–51, 85, 86]. It is noted here that, these selection rules are in qualitative correlation with the selection rules worked out by Warren [1]. Based on the analysis of the numerically calculated diffraction patterns of faulted and twinned *fcc* [51] and hexagonal [88, 89] crystals, Lorentzian and delta-function like profile functions are considered as the uniform profile functions corresponding to faulting and twinning. The  $hkl$  scaling of breadths and

shifts of these uniform profile functions was determined numerically as a function of the density of planar defects, by using the DIFFaX software [42], and is given in data sheets of polynomials available at: <http://metal.elte.hu/~levente/stacking>. Thus the theoretical profile functions of planar defects  $I^{\text{SF}}$  can be given as [51]:

$$I^{\text{SF}}(K) = w_{\delta} I_{hkl}^{\delta}(K) + \sum_{j=1}^N w_L^j I_{L,hkl}^j(K), \quad (10)$$

where  $I_{hkl}^{\delta}$  is the delta-function like component at the exact Bragg position and  $I_{L,hkl}^j$  is the Lorentzian profile function of broadened and shifted sub-reflections, and  $w_{\delta}$  and  $w_L^j$  are the fractions of the different sub-reflection components. The fractions are given by the relative multiplicities of sub-reflection within a  $hkl$  reflection. In *fcc* crystal  $N = 4$  for the first 15 Bragg reflections, in hexagonal crystals  $N = 6$  [88, 89].

The evaluation of faulting and twinning has been incorporated into the convolutional multiple whole profile (CMWP) procedure [84]. The extended convolutional multiple whole profile (eCMWP) method [51] works according to the following principle, also applied in other whole profile fitting procedures, cf. [83, 85]:

$$I^{\text{MEAS}} = I^{\text{S}} \times I^{\text{D}} \times I^{\text{SF}} \times I^{\text{INST}} + BG, \quad (11)$$

where  $I^{\text{MEAS}}$  is the measured and  $I^{\text{INST}}$  the instrumental pattern, and  $BG$  is the background intensity. The  $I^{\text{S}}$ ,  $I^{\text{D}}$ , and  $I^{\text{SF}}$  profile functions or their Fourier transforms are given by Eqs. (4), (7) and (10) in which  $hkl$  scaling is provided by the rule of size anisotropy, the dislocation contrast factors and the scaling scheme worked out for planar defects, respectively.

### 3. Representative applications

#### 3.1 Metals

##### 3.1.1 Evolution of the ultrafine-grained microstructure in metals

Bulk nanocrystalline or ultrafine-grained (UFG) metals are produced either by building up from small structural elements (*e.g.* by electrodeposition or sintering from nanopowders) or by refinement of bulk coarse-grained specimens by severe plastic deformation (SPD). The starting powder of the sintering process can be produced by different methods (*e.g.* sol-gel method, wet chemical synthesis, plasma synthesis, mechanical alloying) which are not discussed here in details. The “building-up” procedures generally result in lower grain size than the SPD methods [91]. On the other hand, the SPD techniques warrant porosity- and contamination-free microstructures. The small subgrain size and the high dislocation density (in the order of  $10^{15} \text{ m}^{-2}$ ) result in very high strength of SPD processed metals and alloys [92, 93]. In the case of severely deformed metals and alloys, X-ray line profile analysis is a unique procedure for determining the very high dislocation density as the establishment of this quantity with good statistics by direct imaging methods, *e.g.* high resolution transmission electron microscopy (HRTEM), requires tre-

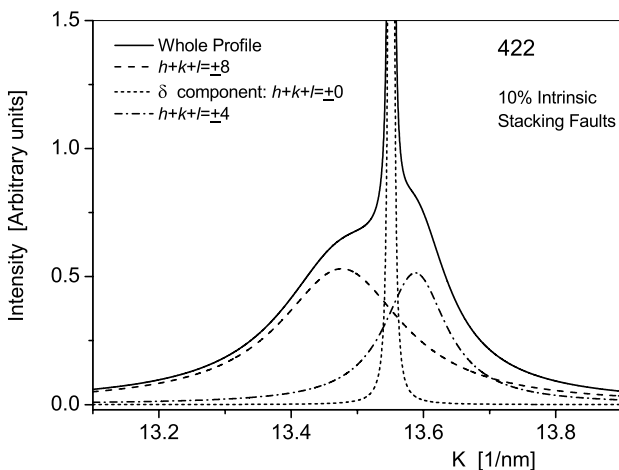


**Fig. 1.** Profiles of the {422} Bragg reflection and sub-reflections corresponding to various  $hkl$  conditions for 10% intrinsic stacking faults, calculated by the DIFFaX [42] software.

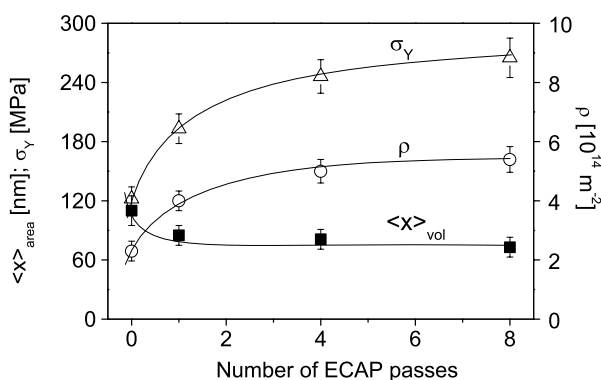


**Fig. 2.** The area-weighted mean crystallite size ( $\langle x \rangle_{\text{area}}$ ), the dislocation density ( $\rho$ ) and the yield strength ( $\sigma_y$ ) as a function of number of ECAP passes for Al-6082 alloy.

mendous efforts. The most frequently used SPD procedure is the equal channel angular pressing (ECAP) as this method results in bulk samples with relatively homogeneous microstructures [94]. One pass through the ECAP die corresponds to an approximate equivalent strain of one [94]. The evolution of the microstructure during ECAP processing has been studied in numerous works [95]. As an example, Fig. 2 shows the area-weighted mean crystallite size,  $\langle x \rangle_{\text{area}}$  and the dislocation density,  $\rho$  for a precipitation hardened Al–Mg–Si alloy, Al-6082, as a function of the number of ECAP passes. Nanosized microstructure,  $\langle x \rangle_{\text{area}} \cong 85$  nm, with relatively high dislocation density,  $4 \times 10^{14} \text{ m}^{-2}$ , was achieved even after 1 pass. Slight increment in the dislocation density and reduction in the crystallite size were observed with further ECAP passes and the parameters of the microstructure saturate after about 4 passes. The yield strength,  $\sigma_y$ , of the ECAP processed Al 6082 specimens was measured at room temperature by compression test and plotted as a function of ECAP passes in Fig. 2. The compression axis was parallel to the output channel axis of the last ECAP pass. Owing to the refinement of the microstructure and the high dislocation density the yield strength increased during ECAP deformation. The yield strength reached its saturation value, about 250 MPa after 4 passes, similar to the dislocation density.

The development of microstructure during ECAP occurs in a similar manner in Al, Al-1%Mg and Al-3%Mg specimens as for the Al 6082 sample [93]. The saturation values of the crystallite size are approximately 300, 90 and 70 nm for Al, Al-1%Mg and Al-3%Mg, respectively. This means that ECAP results in nanosized microstructure only in the cases of Al alloys but not for pure Al. In the latter case the microstructure can be regarded as ultrafine-grained where the crystallite size is between 100 and 1000 nm. For pure Al the dislocation density reached its maximum value also even after the first pass, about  $2 \times 10^{14} \text{ m}^{-2}$ . At the same time, for Al–Mg alloys the saturation occurs only at 4 passes similar to Al 6082 [93]. The maximum value of the dislocation density are  $3.9 \times 10^{14}$  and  $23 \times 10^{14} \text{ m}^{-2}$  for Al-1%Mg and Al-3%Mg, respectively, which are much higher than that for pure Al. These phenomena can be explained by the effect of Mg solute atoms on the dislocation mobility. The Mg atoms impede the motion of dislocations in Al matrix which hinders the annihilation of dislocations during deformation leading to an increase in the disloca-

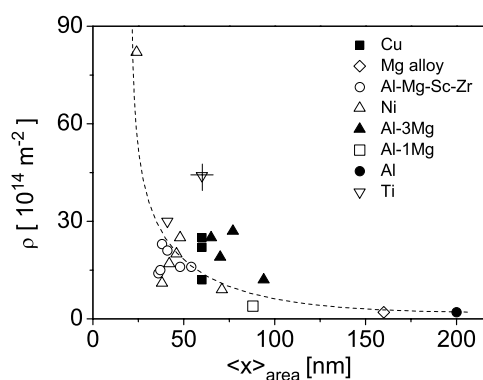


**Fig. 3.** The dislocation density ( $\rho$ ) versus the area-weighted mean crystallite size ( $\langle x \rangle_{\text{area}}$ ) for bulk nanocrystalline and ultrafine-grained metals. The solid horizontal and vertical lines at the down-triangle indicate the experimental uncertainties.

tion density. The reduced recovery rate is responsible also for the fact that saturation of dislocation density is achieved only at higher strain values. As the grain-refinement in SPD metals occurs usually by the arrangement of dislocations into cell boundaries, the higher dislocation density results in the decrease of crystallite size for higher Mg concentration.

### 3.1.2 Correlation between the dislocation density, the crystallite size and the grain size in ultrafine-grained metals

Increasing the strain during SPD procedures, the increase of the dislocation density and the reduction of the crystallite size occur simultaneously. The correlation between the two quantities is shown in Fig. 3 for bulk UFG metals produced by SPD methods, *i.e.* by ECAP and high pressure torsion-HPT. The different values for one composition correspond to different strain values achieved by SPD. The data point related to the highest dislocation density of  $82 \times 10^{14} \text{ m}^{-2}$  corresponds to the nanocrystalline Ni specimen produced by electrodeposition. It can be concluded that, although there is no strict correlation between the crystallite size and the dislocation density of the UFG metals processed by SPD procedures, the higher dislocation density is associated with smaller crystallite size. This is a consequence of the fact that the mechanism of grain-refinement in SPD materials is the formation of low energy dislocation configurations, *e.g.* dislocation walls. It seems that this mechanism limits the lowest achievable value of the crystallite size to about 30 to 40 nm, especially in Cu, Ni or Fe, or usually in metals in which the grain refinement is carried out at homologous temperatures not higher than about  $0.25 \times T_m$ , where  $T_m$  is the melting temperature.

In Fig. 4 the grain size determined from TEM images are compared with the mean crystallite size,  $\langle x \rangle_{\text{area}}$ , obtained from X-ray line profile analysis for SPD processed metals and alloys. The mean crystallite size determined by X-rays is generally lower than the grain size observed in the TEM images which has been already reported for other SPD materials previously [19, 68, 96]. This difference may be explained by the hierarchical microstructure of SPD metals. The grains in SPD materials are divided into subgrains and/or dislocation cells which are separated

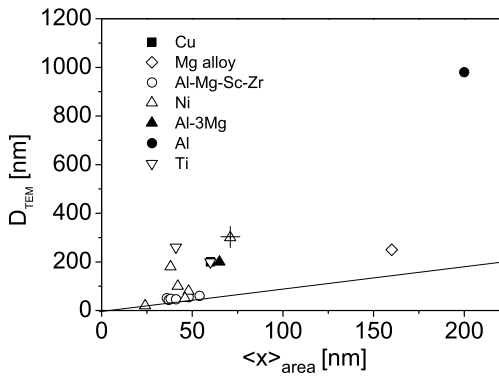


**Fig. 4.** The grain size determined from TEM images ( $D_{\text{TEM}}$ ) vs. the area-weighted mean crystallite size,  $x_{\text{area}}$ , obtained from X-ray line profile analysis for SPD processed metals and alloys. The solid line has a slope equal to one. The solid horizontal and vertical lines at the up-triangle indicate the experimental uncertainties.

from each other by low angle grain boundaries. The crystallite size in SPD metals obtained by X-ray diffraction is equivalent to the mean size of domains which scatter X-rays coherently. Consequently, X-ray diffraction makes a difference between the dislocation cells which are separated from each other by small misorientation, typically under 1–2 degrees. At the same time it was found previously [68, 96] that these dislocation cells can only be observed separately by electron microscopy if highly magnified TEM images are studied very carefully. The agreement between the distributions of cell size determined by TEM and crystallite size obtained by X-ray line profile analysis is demonstrated in Fig. 5 for Ti processed by 8 ECAP passes [96]. The usual TEM investigation of SPD metals gives the grain size which is higher than the dislocation cell size obtained by X-ray diffraction peak profile analysis. To obtain a detailed image of the microstructure of SPD materials, the simultaneous application of X-ray diffraction and TEM is necessary. TEM studies showed that the minimum grain size in metals achievable by SPD is about 100–200 nm therefore these materials are rather called as ultrafine-grained instead of nanocrystalline. However, the size of subgrains or cells inside the grains may be as small as 40 nm as discussed above.

It should be noted, that for real nanocrystalline metals where the grain size (not the crystallite or domain size!) is of several tens of nanometers, the ex-situ investigations did not show dislocations inside the grains. These materi-

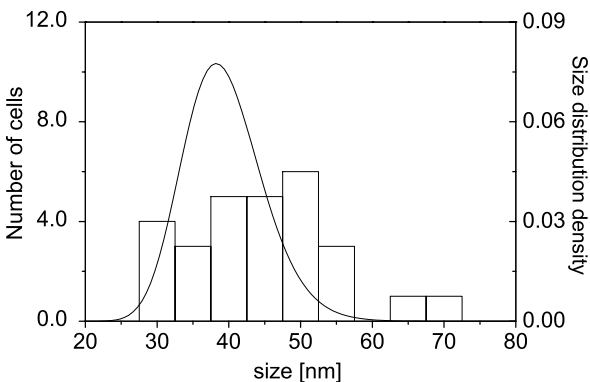


**Fig. 5.** The distribution of cell size determined by TEM and that of crystallite size obtained by X-ray line profile analysis for Ti processed by 8 ECAP passes [96].

als are usually processed by condensation or deposition methods which are essentially different from SPD. At the same time, in-situ TEM observations showed dislocation activity during deformation of electrodeposited, fully dense, nanocrystalline Ni with an average grain size of  $\sim 30$  nm [97]. This means that in spite of the lack of storage of dislocations inside the grains, the plastic deformation may be mediated by dislocations even in nanocrystalline materials. It was also shown that beside dislocation motion, other mechanisms, e.g. grain boundary sliding also contributes to deformation of nanomaterials [98–102].

### 3.1.3 Dislocation structure in nanocrystalline hexagonal metals

For obtaining fine-grained microstructure with high dislocation density SPD procedures were applied also to hexagonal metals, e.g. on commercially pure Ti (CP Ti) [96] and AZ91 Mg alloy [35]. Generally, the SPD processes on hexagonal materials are carried out at elevated temperatures because of brittleness at room temperature. In hexagonal nanomaterials X-ray line profile analysis enables the determination not only the density of dislocations but their Burgers vector population. The eleven dislocation slip systems in hexagonal materials can be classified into three groups based on their Burgers vectors:  $b_1 = \frac{1}{3}\langle 2110 \rangle$  ( $\langle a \rangle$ -type),  $b_2 = \langle 0001 \rangle$  ( $\langle c \rangle$  type) and  $b_3 = \frac{1}{3}\langle 2113 \rangle$  ( $\langle c+a \rangle$  type). There are 4, 2 and 5 slip systems in the  $\langle a \rangle$ ,  $\langle c \rangle$  and  $\langle c+a \rangle$  Burgers vector groups, respectively. In

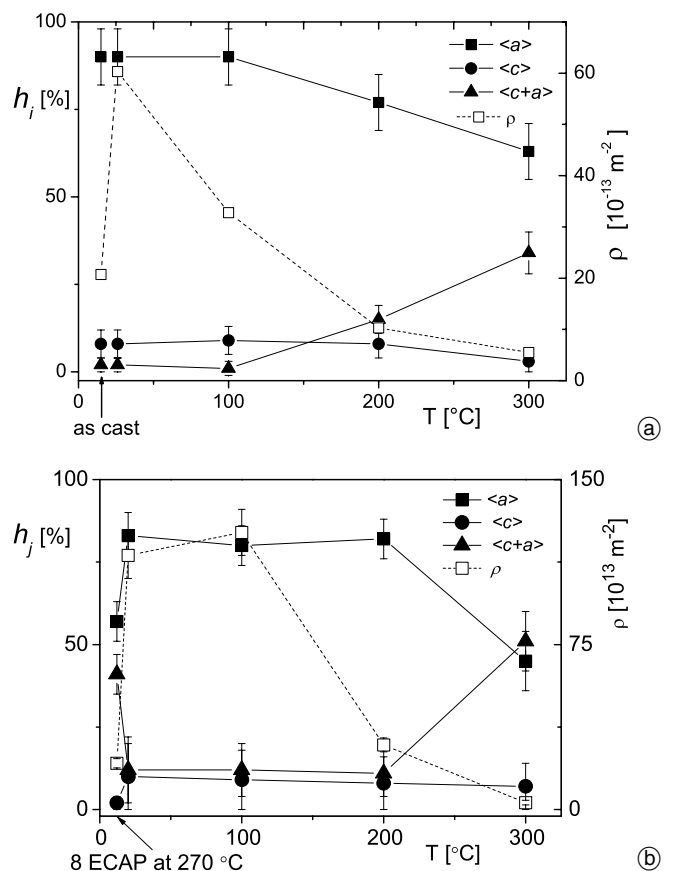


**Fig. 6.** The dislocation density ( $\rho$ ) and the relative fractions of Burgers vectors ( $h_j$ ) for as-cast Mg (a) and ultrafine-grained AZ91 Mg alloy processed by 8 ECAP at 270 °C (b) as a function of temperature of deformation.

commercially pure Ti specimen processed by 8 ECAP passes at 400–450 °C, the dislocation density obtained from X-ray line profile analysis is  $44 \times 10^{14} \text{ m}^{-2}$ . The relative fractions of the  $\langle a \rangle$ ,  $\langle c \rangle$  and  $\langle c + a \rangle$  Burgers vectors are 62%, 0–4% and 32–36%, respectively. The abundance of  $\langle a \rangle$ -type dislocations besides the  $\langle c \rangle$ - and  $\langle c + a \rangle$ -type dislocations has been also found for SPD processed Mg alloys [35]. The relatively high fraction of  $\langle c + a \rangle$  dislocations in hexagonal materials processed by ECAP can be attributed to the high temperature of deformation. Theoretical calculations and TEM observations for hexagonal metallic materials suggest the activation of  $\langle c + a \rangle$  dislocations by strong deformation at elevated temperatures [102]. At room temperature the critical resolved shear stress of pyramidal  $\langle c + a \rangle$  dislocations is about five times larger than that for basal slip [98], but this value decreases with increasing temperature. The development of the dislocation density and the Burgers vector population as a function of temperature of deformation are compared for coarse-grained Mg and ultrafine-grained AZ91 Mg alloy processed by high temperature ECAP in Fig. 6. The relative fraction of the  $\langle c + a \rangle$  dislocations is high even in the initial state obtained after ECAP-processing as it was carried out at high temperature (270 °C). The dislocation density is higher for any deformation temperature in the case of ultrafine-grained material because of the higher defect density in the starting state processed by ECAP. The increase of the population of  $\langle c + a \rangle$  dislocations occurs at higher temperature for the ultrafine-grained sample than for the as-cast sample. This is probably due to fact that for ultrafine grained materials grain boundary sliding also contributes to the macroscopic deformation beside the sliding of dislocations therefore the driving force to activate  $\langle c + a \rangle$  dislocation is less than for coarse grained materials.

### 3.1.4 Planar faults in nanocrystalline metallic materials

The eCMWP procedure described above is applied to evaluate planar fault densities together with dislocation densities and crystallite size in nanocrystalline and submicron grain-size copper specimens. Bulk nanocrystalline copper specimens were prepared by inert gas condensation (IGC) and hot compaction at Argonne National Laboratory [30, 103–106]. They are denoted as O<sub>2</sub>-IS, P<sub>2</sub>-IS, and N<sub>2</sub>-IS in the as-prepared state (initial state) and P<sub>2</sub>-T and N<sub>2</sub>-C after tensile and compression tests, respectively. The notations are the same as in Weertman and Sanders [104], Sanders [105], Sanders *et al.* [106] and Ungár *et al.* [30, 103]. Submicron grain-size copper samples were prepared by ECAP either in the laboratory of Professor Valiev [107] or in the laboratory of Professor Estrin [108] denoted as ECAP(a) or ECAP(b), respectively. The twin densities,  $\beta$  are shown as a function of the area-weighted mean crystallite size,  $\langle x \rangle_{\text{area}}$  for the different nanocrystalline and submicron grain size specimens in Fig. 7. The values of  $\beta$  gives the probability of finding a twin boundary between two neighboring (111) lattice planes. The dashed line is to guide the eye. It can be seen that when the subgrain size is larger than about 40 nm the twin density is close to zero, within experimental error. At subgrain-size values smaller than about 40 nm the twin

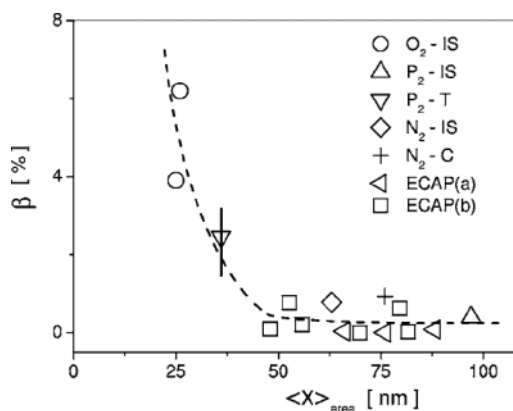


**Fig. 7.** The twin density as a function of the area-weighted mean crystallite size,  $\langle x \rangle_{\text{area}}$ , for different nanocrystalline Cu specimens. Inert gas condensed and compacted specimens: O<sub>2</sub>-IS, P<sub>2</sub>-IS, P<sub>2</sub>-T, N<sub>2</sub>-IS, and N<sub>2</sub>-C. Submicron grain-size samples deformed by ECAP: ECAP (a) open left triangles and ECAP (b) open squares, respectively. The dashed line is to guide the eye. The solid vertical line indicates the experimental uncertainty [30, 103–108].

density increases sharply and reaches values up to 6%. On the basis of the model calculations and the experimental values of stacking fault energy in Cu, Zhu *et al.* [109] suggest 40 nm as the critical grain size below which deformation proceeds by twinning instead of dislocation glide. Figure 7 shows an excellent correlation with this suggestion: when the area-weighted mean crystallite size is larger than about 40 nm the twin density, within experimental error, is close to zero. It should be noted that this limiting value of crystallite size may change with the stacking fault energy (SFE) of the metal. It has been shown [110] that for Cu-10 wt% Zn where the SFE is about half of that for pure Cu, the severe plastic straining of HPT results in a relatively high twin density of 4.8% even for the crystallite size of 50 nm. Comparing pure Cu and Cu-10 wt% Zn specimens, the lower SFE results in also a lower crystallite size (70 nm was determined for Cu) and 2.5 times higher dislocation density [110].

### 3.2 Ceramics

Dense nanocrystalline ceramic materials are usually produced by sintering of nanopowders. The effect of the size distribution of the starting ceramic powders and the sintering conditions (*e.g.* temperature and pressure) on the microstructure of the compacted bulk material has been studied by X-ray line profile analysis in several papers [9, 16, 111]. Louër *et al.* [111] have determined the shape, size and size distribution of crystallites in nanocrystalline ZnO powder synthesized by thermal decomposition of zinc hydroxynitrate. Although the line breadths show a strong  $hkl$  dependence, the harmonic pairs of reflections, *e.g.* 100–300 and 002–004 were identical within experimental errors. These observations were attributed to the shape anisotropy of the crystallites. In the quantitative evaluation of the Fourier transforms of the profiles, the crystallites are modelled by cylinders. It was found that the axis of the cylinder was parallel to the hexagonal  $c$  axis and the average diameter and height were 11 and 24 nm, respectively. TEM micrographs have confirmed the same shape anisotropy and average size values, although they showed that

the real shape of the crystallites is prism with irregular hexagonal cross section.

Bulk ultrafine-grained tungsten-carbide specimen was produced by ball-milling of submicron size powder and subsequent sintering at high temperature (1420 °C). The crystallite size distribution of nanopowders obtained by ball-milling and the bulk specimen produced by sintering were studied by X-ray line profile analysis [9]. The line breadths decreased down to about one-third during sintering as a consequence of the grain-growth at high temperature consolidation. The good agreement between the crystallite size distribution determined by line profile analysis and TEM has been observed for the sintered tungsten-carbide sample [9]. The good correlation between the mean crystallite size determined by X-ray diffraction, about 2.4 nm, and that obtained from TEM micrographs, about 3.5 nm, was also observed for a CeO<sub>2</sub> ceramic powder [16]. This powder was prepared by decomposition of Ce<sub>2</sub>O(NO<sub>3</sub>)<sub>6</sub> · H<sub>2</sub>O in nitrogen atmosphere at 230 °C. It was found that the strain contribution to peak broadening is also negligible for this material.

The crystallite size in silicon nitride ceramic powders determined by X-ray line profile analysis were also compared with TEM observations and specific surface area measurements [11]. A silicon nitride powder was produced by nitridation of silicon and subsequent milling [11]. The area weighted mean crystallite size,  $\langle x \rangle_{\text{area,X-ray}} = 62(5)$  nm, agrees well with the area weighted mean particle size calculated from the specific surface area determined by the Brunauer-Emmett-Teller (BET) method  $\langle x \rangle_{\text{area,BET}} = 71(5)$  nm. The crystallite size distribution was also in very good agreement with that obtained from TEM micrographs. Another Si<sub>3</sub>N<sub>4</sub> powder was prepared by gas-phase synthesis of silicon-tetrachloride and ammonia in thermal plasma reactor and post-crystallization at 1500 °C for 2 h. It was found that the mean size obtained from line profile analysis,  $\langle x \rangle_{\text{area,X-ray}} = 93(5)$  nm was in good agreement with that determined by BET method  $\langle x \rangle_{\text{area,BET}} = 94(5)$  nm. It was found that the TEM particle size distribution contained somewhat smaller particles than those in the crystallite size distribution obtained from line profile analysis. This is unusual among the comparative studies of X-ray and TEM sizes since in general the grain size determined by X-ray is smaller than that established

by TEM. The phenomena can be explained by the smaller amorphous grains in the powder.

Figure 8 shows the grain size determined by TEM for ceramic materials discussed here versus the area-weighted mean crystallite size obtained by X-ray line profile analysis. It can be concluded that for nanocrystalline ceramic materials the two size values agree well. This means that usually the grains or particles in the bulk or powder ceramic materials, respectively, are single crystals, *i.e.* in contrast with metals they are not divided into smaller domains, *e.g.* by dislocation cell-walls. In multiple-phase ceramic materials where the particles consists of crystallites of different phases, the particle size can be larger than the crystallite as shown in the case of zirconia ceramics [112]. In ceramic powders containing amorphous fraction the crystallite size can be smaller or higher than the particle size.

### 3.3 Diamond and silicon carbide

Bulk nanostructured diamond may be consolidated from nanopowders under high pressure and high temperature conditions. From the agreement between the particle size distributions of the starting powders obtained by line profile analysis and BET method, it was concluded that for the size below 30 nm, the diamond particles are single crystals similarly as for ceramic powders [113]. The Williamson-Hall plots show that these particles are dislocation free but they contain significant amount of planar faults [113]. The diamond powders with the particle size higher than 30 nm contains dislocations and their density increases during sintering procedure. Bulk ultrafine grained diamond can be also processed by sintering of micron-sized powders. During consolidation at high pressure and temperature, dislocations are formed and the grains are divided into subgrains or dislocation cells, similarly as in metals by severe plastic deformation [113]. The dislocation formation is induced by the contact shear stresses exerted by the edges of neighboring particles in the compressed powder.

Silicon carbide is also frequently used as a functional and structural material at high temperatures. Nanocrystalline SiC offers very high strength either as a binding phase in diamond composites or as a single phase material even at high temperatures [114]. Ultrafine grained bulk SiC samples are usually fabricated from nanopowders by sintering at high pressures and temperatures. It is expected that the microstructure of sintered SiC can be tailored by the proper selection of these two parameters [114].

To study the effect of the sintering conditions on the microstructure, bulk nanocrystalline SiC specimens were sintered from SiC nanopowder with nominal grain size of 30 nm. The sintering procedure was carried out at temperatures of 1400, 1600 and 1800 °C. At each temperature, specimens were sintered at pressures of 2, 4 and 5.5 GPa. This process gave nine bulk sintered SiC samples, in addition to the initial powder. An additional specimen was produced at 1800 °C and at a very high sintering pressure of 8 GPa. The lattice defect structure and the crystallite size are studied by X-ray line profile analysis and transmission electron microscopy. For revealing the

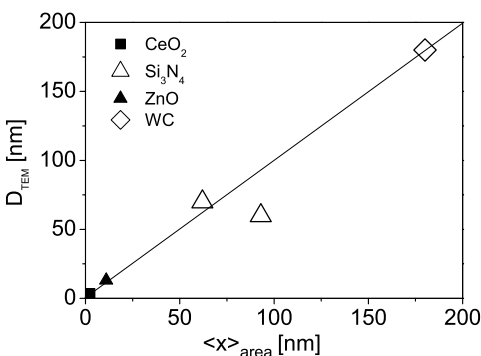


**Fig. 8.** The grain size determined from TEM images ( $D_{\text{TEM}}$ ) vs. the area-weighted mean crystallite size,  $x_{\text{area}}$ , obtained from X-ray line profile analysis for nanostructured ceramic materials. The solid line has a slope equal to one. The size of the symbols represents the uncertainty of data.

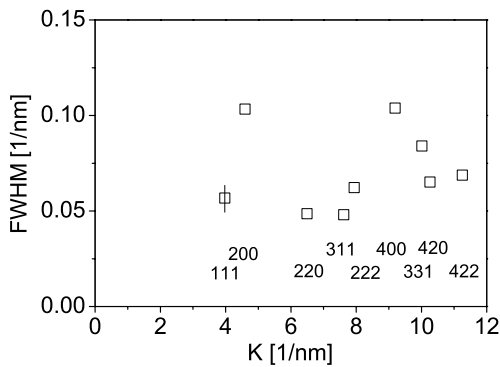


**Fig. 9.** The Williamson-Hall plot of nanocrystalline SiC sintered at 5.5 GPa and 1400 °C. The solid vertical line indicates the experimental uncertainty.

type of lattice defects in the microstructure, the Full Width at Half Maximum (FWHM) was plotted as a function of the length of the diffraction vector in the Williamson-Hall plot. The character of the Williamson-Hall plots are different for the samples sintered at different conditions. For the initial powder and the specimens sintered at pressures lower than 4 GPa and temperatures below 1600 °C, the FWHM values of the *111/222* and *200/400* reflection pairs are order-independent indicating that line broadening, in this case, is mainly caused by small crystallite size and/or planar faults. A typical example of such type Williamson-Hall plots is shown in Fig. 9 where the FWHM data are plotted for the specimen sintered at 5.5 GPa and 1400 °C.

At the same time, for the SiC specimen sintered at higher pressures and temperatures, *e.g.* 5.5 GPa and 1800 °C, the breadths of harmonic pairs of reflections are different, *i.e.* there is a strong order-dependence of the FWHM values, as shown in Fig. 10. This demonstrates the existence of lattice strains in the crystallites. If the lattice strains are caused by dislocations, the peak breadths have a specific dependence on *hkl* indices [25]. In this case the FWHM values follow a nonmonotonous line with increasing *K* in the Williamson-Hall plot, *i.e.* the breadth of a peak is smaller than that for another peak at smaller *K* value [65]. This type of behavior can be observed in Fig. 10 for *400* and *331* reflections. Assuming the most common dislocation slip system in SiC, *i.e.*  $\langle 110 \rangle \{ 111 \}$ , with the Burgers vector  $\mathbf{b} = a/2 \langle 110 \rangle$ , the anisotropic strain broadening has been rationalized by the average

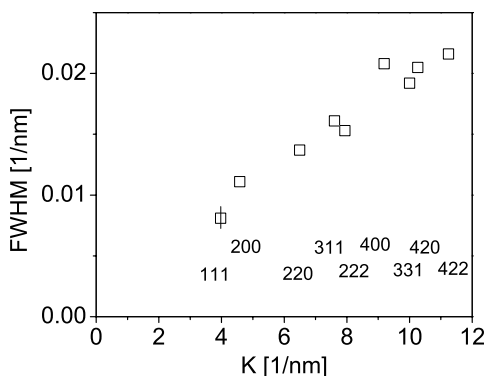


**Fig. 10.** The Williamson-Hall plot for nanocrystalline SiC sintered at 5.5 GPa and 1800 °C. The solid vertical line indicates the experimental uncertainty.

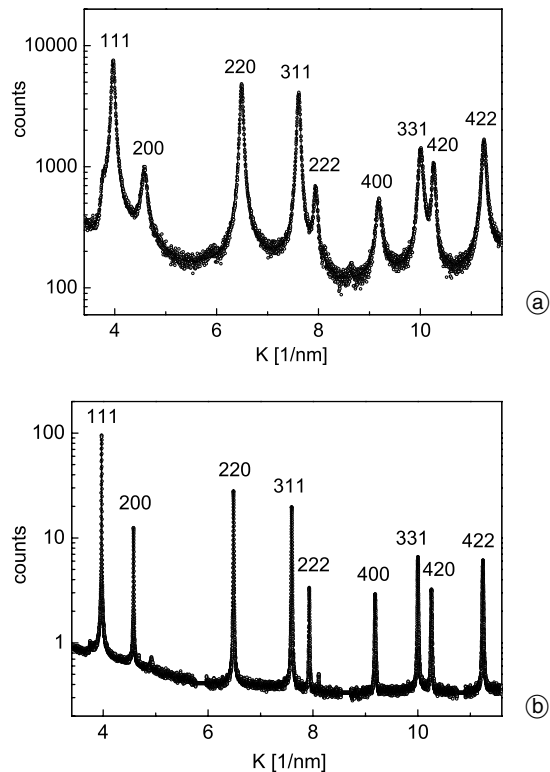


**Fig. 11.** The eCMWP fitting of the patterns for the samples sintered at 5.5 GPa and temperatures of (a) 1400 °C and (b) 1800 °C. Open circles and solid line represent the measured and the fitted patterns, respectively.

contrast factors,  $\bar{C}$ , in the *modified* Williamson-Hall plot, see *e.g.* in Fig. 4b in [114], which indicates that strain broadening of the profiles is caused by dislocations.

For the quantitative characterization of lattice defect structure and crystallite size in nanostructured SiC samples, the X-ray patterns of the initial powder and the sintered specimens were evaluated by the eCMWP fitting method [114]. Typical examples of the fitting for the samples sintered at 5.5 GPa and temperatures of 1400 °C and 1800 °C are shown in Fig. 11. The line profile analysis showed that the crystallite size increases during sintering. The grain-growth is higher for higher temperature or pressure of sintering. At the same time at 1800 °C the very high pressure, 8 GPa, impeded the increase of the crystal-

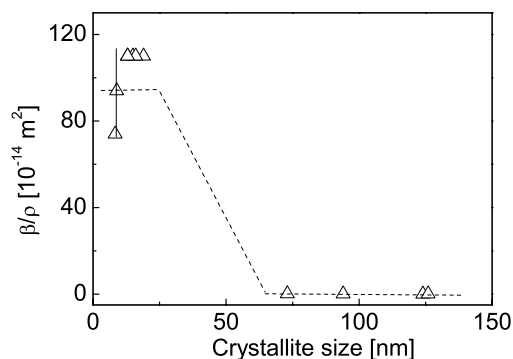


**Fig. 12.** The ratio of the twin density and the dislocation density ( $\beta/\rho$ ) as a function of the crystallite size for nanocrystalline SiC specimens sintered at different conditions. The solid vertical line indicates the experimental uncertainty. The dashed line shows a reasonable correlation suggested by the datapoints.

lite size. Examination of the TEM images confirmed that conclusion. A correlation between the crystallite size and the lattice defect structure has been established. Figure 12 shows the ratio of the twin density and the dislocation density ( $\beta/\rho$ ) as a function of the crystallite size for nanocrystalline SiC specimens sintered at different conditions. It can be concluded that the increase of the crystallite size is accompanied by the reduction of planar fault probability and by the increase of the dislocation density. This result is also in line with previous observations for Cu and Cu–Zn alloys discussed above in this paper. The critical value of crystallite size for nc-SiC, where dislocations are abundant instead of planar faults, is estimated to be between 25 and 70 nm.

### 3.4 Polymers

The effect of plastic deformation on the lattice defect structure in nanostructured monoclinic *a*-phase isotactic polypropylene (PP) was studied by X-ray line profile analysis [115]. The specimens were plastically deformed by rolling to different strain values up to 49.6%. For the coherently scattering domain size, or “apparent crystallite size”, the evaluation yields a continuous decrease with increasing plastic deformation. The resulting domain sizes lie between 20 nm for the undeformed and 15 nm for the deformed specimen, where  $\varepsilon_{\text{true}} = 50\%$ . This value is in good correlation with the lamella thickness of polypropylene [115]. The Williamson-Hall plot in Fig. 13 shows a strong order dependence of peak breadths. Using the average dislocation contrast factors,  $\bar{C}$ , the FWHM values can be arranged along a smooth curve in the modified Williamson-Hall plot, as it can be seen in Fig. 14. This means that the lattice defects in melt-crystallised and plastically deformed polypropylene have the same type of strain field as for dislocations, therefore we can call these defects as dislocations.

The modified Williamson-Hall plot was used only for the examination of the source of lattice strain in the microstructure. The dislocation density was evaluated by profile fitting method (CMWP). It was found that the dislocation density increases with deformation, as it can be seen in Fig. 15. The dislocation densities of plastically deformed

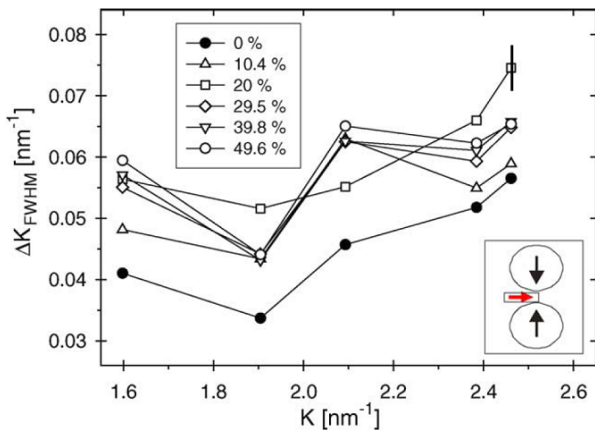


**Fig. 13.** Classical Williamson-Hall plot for polypropylene peaks (1 1 0), (0 4 0), (1 3 0), (0 5 0) and (0 4 1) deformed by rolling up to  $\varepsilon_{\text{true}} = 49.6\%$ . The solid vertical line indicates the experimental uncertainty.

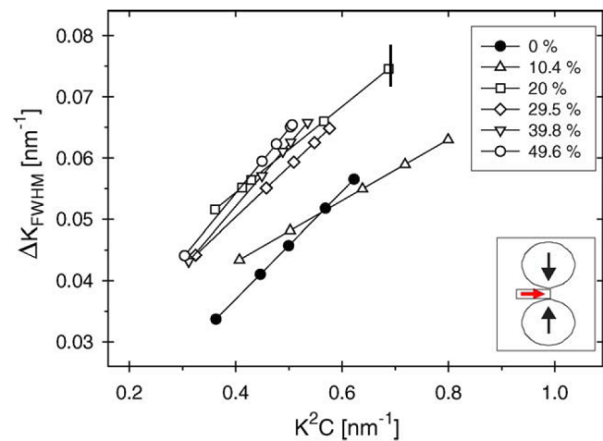


**Fig. 14.** Modified Williamson-Hall plot for the same sample and peaks as in Fig. 13. The solid vertical line indicates the experimental uncertainty.

PP are between  $10^{16}$  and  $10^{17} \text{ m}^{-2}$ . The reported dislocation densities in polypropylene are considerably higher than the values for common metals. An explanation is the long-chain nature of the macromolecules which cause additional constraints when polymer crystals develop. This, in some natural way, leads to the strong production of dislocations already in the undeformed materials [116]. The higher initial dislocation density might yields higher number of sources for dislocation generation during deformation compared to metallic materials.

## 4. Summary

The fundamentals of the method of X-ray line profile analysis is discussed in terms of: (i) strain anisotropy, and the dislocation model of strain anisotropy, (ii) the qualitative information provided by the different breadth methods, especially the Williamson-Hall and *modified* Williamson-Hall plots and the *modified* Warren-Averbach procedure, (iii) the more sophisticated and more quantitative methods of whole profile and whole pattern fitting procedures. The efficiency of the procedure is demonstrated by discussing the defect structures in metals, ceramics, diamond and SiC nanocrystals and polymers. It is shown that, especially in

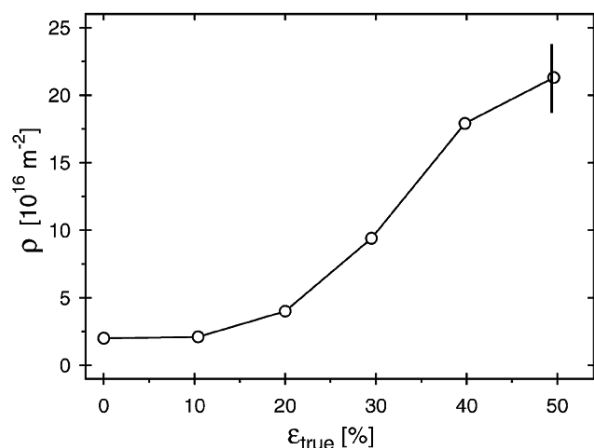


**Fig. 15.** Dislocation density versus the true strain for the rolled polypropylene specimens. The solid vertical line indicates the experimental uncertainty.

bulk metallic submicron grain size and nanomaterials processed by plastic deformation, the X-ray crystallite size is in best correlation with the subgrain size or dislocation cell size provided by TEM or HRTEM. In the case of powder or sintered bulk ceramics X-ray crystallite size is in good agreement with TEM particle or grain size, respectively. It has been shown that twinning and faulting can readily be determined together with the dislocation structure and size properties. It was found that in submicron grain size and nanocrystalline copper twinning becomes substantial when the crystallite size is smaller than about 40 nm. In nanocrystalline SiC, starting from a twinned nano-powder, twinning has been enhanced when crystallite size remained small during sintering, whereas, grain coarsening caused by sintering is accompanied by increased dislocation activity at the cost of twinning. In polypropylene X-ray line profile analysis has provided extremely large dislocation densities in good correlation with the small lamella thickness in this structure.

*Acknowledgments.* The authors are grateful for the financial support of the Hungarian National Science Foundation, OTKA T46990, T67692 and F47057. This work was supported by the Bolyai János Research Scholarship of the Hungarian Academy of Sciences.

## References

- [1] Warren, B. E.: X-ray Studies of Deformed Metals. *Progr. Metal Phys.* **8** (1959) 147–202.
- [2] Wilson, A. J. C.: X-Ray Optics, the Diffraction of X-Rays by Finite and Imperfect Crystals. London, Methuen, 1962.
- [3] Delhez, R.; de Keijser, Th. H.; Mittemeijer, E. J.: Determination of crystallite size and lattice-distortions through X-ray-diffraction line-profile analysis – Recipes, methods and comments. *Fresenius Z Anlz. Chem.* **312** (1982) 1–16.
- [4] Louër, D.; Auffrédic, J. P.; Langford, J. I.; Ciosmak, D.; Niepce, J. C.: A precise determination of the shape, size and distribution of size of crystallites in zinc oxide by X-ray line-broadening analysis. *J. Appl. Cryst.* **16** (1983) 183–191.
- [5] Langford J. I.; Louër, D.: High-resolution powder diffraction studies of copper(II) oxide. *J. Appl. Cryst.* **24** (1991) 149–155.
- [6] Langford, J. I.; Boultif, A.; Auffrédic, J. P.; Louër, D.: The use of pattern decomposition to study the combined X-ray diffraction effects of crystallite size and stacking faults in ex-oxalate zinc oxide. *J. Appl. Cryst.* **26** (1993) 22–33.
- [7] Balzar, D.; Ledbetter, H.: Voigt-function modeling in Fourier analysis of size- and strain-broadened X-ray diffraction peaks. *J. Appl. Cryst.* **26** (1993) 97.
- [8] Krill, C. E.; Birringer, R.: Estimating Grain-Size Distributions in Nanocrystalline Materials from X-Ray Diffraction Profile Analysis. *Phil. Mag.* **77** (1998) 621–640.
- [9] Ungár, T.; Borbély, A.; Goren-Muginstein, G. R.; Berger S.; Rosen, A. R.: Particle-size, size distribution and dislocations in nanocrystalline tungsten-carbide. *Nanostructured Materials* **11** (1999) 103–113.
- [10] Langford, J. I.; Louër D.; Scardi, P.: Effect of a crystallite size distribution on X-ray diffraction line profiles and whole-powder-pattern fitting. *J. Appl. Cryst.* **33** (2000) 964–974.
- [11] Gubicza, J.; Szépvölgyi, J.; Mohai, I.; Zsoldos L.; Ungár, T.: Particle size distribution and the dislocation density determined by high resolution X-ray diffraction in nanocrystalline silicon nitride powders. *Mat. Sci. Eng. A280* (2000) 263–269.
- [12] Scardi, P.; Leoni, M.: Diffraction line profiles from polydisperse crystalline systems. *Ata Cryst.* **A57** (2001) 604–613.
- [13] Szépvölgyi, J.; Mohai, I.; Gubicza, J.: Atmospheric ageing of nano-sized silicon nitride powders. *J. Mater. Chem.* **11** (2001) 859–863.
- [14] Rafaja, D.; Klemm, V.; Schreiber, G.; Knapp, M.; Kužel, R.: Interference phenomena observed by X-ray diffraction in nanocrystalline thin films. *J. Appl. Cryst.* **37** (2004) 613–620.
- [15] Leoni, M.; Scardi, P.: Nanocrystalline domain size distributions from powder diffraction data. *J. Appl. Cryst.* **37** (2004) 629–634.
- [16] Balzar, D.; Audebrand, N.; Daymond, M. R.; Fitch, A.; Hewat, A.; Langford, J. I.; Le Bail, A.; Louër, D.; Masson, O.; McCowan, C. N.; Popa, N. C.; Stephens, P. W.; Toby, B. H.: Size-strain line-broadening analysis of the ceria round-robin sample. *J. Appl. Cryst.* **37** (2004) 911–924.
- [17] Pielaszek, R.: FW1/5/4/5M method for determination of the grain size distribution from powder diffraction line profile. *J. Alloys Comp.* **382** (2004) 128–132.
- [18] Shen, T. D.; Schwarz, R. B.; Thompson, J. D.: Soft magnetism in mechanically alloyed nanocrystalline materials. *Phys. Rev.* **B72** (2005) 014431.
- [19] Ungár, T.; Tichy, G.; Gubicza J.; Hellmig, R. J.: Correlation between subgrains and coherently-scattering-domains. *Powder Diffr.* **20** (2005) 366–375.
- [20] Rafaja, D.; Poklad, A.; Klemm, V.; Schreiber, G.; Heger, D.; Šíma, M.; Dopita, M.: Some consequences of the partial crystallographic coherence between nanocrystalline domains in Ti–Al–N and Ti–Al–Si–N coatings. *Thin Solid Films* **514** (2006) 240–249.
- [21] Krivoglaz, M. A.: X-ray and Neutron Diffraction in Nonideal Crystals, Springer-Verlag, Berlin, Heidelberg, New York, 1996.
- [22] Wilkens, M.: Determination of density and distribution of dislocations in deformed single crystals from broadened X-ray diffraction profiles. *phys. stat. sol. (a)* **2** (1970) 359–370.
- [23] Wilkens, M.: Fundamental Aspects of Dislocation Theory (Eds. J. A. Simmons, R. de Wit, R. Bullough) p. 1195. *Nat. Bur. Stand. Spec. Publ. Vol. II. No. 317.* Washington DC, USA, 1970.
- [24] Wilkens, M.: Proc. 8th Int. Conf. Strength Met. Alloys (ICSMA 8). Tampere, Finland. (Eds. P. O. Kettunen, T. K. Lepistö, M. E. Lehtonen) p. 47. Pergamon Press, 1988.
- [25] Ungár, T.; Borbély, A.: The effect of dislocation contrast on X-ray line broadening: a new approach to line profile analysis. *Appl. Phys. Lett.* **69** (1996) 3173–3175.
- [26] Groma, I.; Ungár T.; Wilkens, M. J.: Asymmetric X-ray-line broadening of plastically deformed crystals.1. Theory. *Appl. Cryst.* **21** (1988) 47–53.
- [27] Groma, I.: X-ray line broadening due to an inhomogeneous dislocation distribution. *Phys. Rev.* **B57** (1998) 7535–7542.
- [28] Kuzel Jr., R.; Klimanek, P.: X-ray diffraction line broadening due to dislocations in non-cubic materials. 2. The case of elastic-anisotropy applied to hexagonal crystals. *J. Appl. Cryst.* **21** (1988) 363–368.
- [29] Kuzel Jr., R.; Klimanek, P.: X-ray diffraction line broadening due to dislocations in non-cubic materials. 3. Experimental results for plastically deformed zirconium. *J. Appl. Cryst.* **22** (1989) 299–307.
- [30] Ungár, T.; Ott, S.; Sanders, P.; Borbély, A.; Weertman, J. R.: Dislocations, grain size and planar faults in nanostructured copper determined by high resolution X-ray diffraction and a new procedure of peak profile analysis. *Acta mater.* **46** (1998) 3693–3699.
- [31] Ungár, T.; Tichy, G.: The effect of dislocation contrast on X-ray line profiles in untextured polycrystals. *phys. stat. sol. (a)* **147** (1999) 425–434.
- [32] Ungár, T.; Leoni, M.; Scardi, P.: The dislocation model of strain anisotropy in whole powder-pattern fitting: the case of an Li–Mn cubic spinel. *J. Appl. Cryst.* **32** (1999) 290–295.
- [33] Máthi, K.; Nyilas, K.; Axt, A.; Cernatescu, I. D.; Ungár, T.; Lukác, P.: The evolution of non-basal dislocations as a function of deformation temperature in pure magnesium determined by X-ray diffraction. *Acta Mater.* **52** (2004) 2889–2894.
- [34] Cordier, P.; Ungár, T.; Zsoldos, L.; Tichy, G.: Dislocation creep in MgSiO<sub>3</sub> perovskite at conditions of the Earth's uppermost lower mantle. *Nature* **428** (2004) 837–840.
- [35] Máthi, K.; Gubicza, J.; Nam, N. H.: Microstructure and mechanical behavior of AZ91 Mg-alloy processed by Equal Channel Angular Pressing. *J. Alloys Comp.* **394** (2005) 194–199.
- [36] Ungár, T.; Castelnaud, O.; Ribárik, G.; Drakopoulos, M.; Bechade, J. L.; Chauveau, T.; Snigirev, A.; Snigireva, I.; Schroer, C.; Bacroix, B.: Grain to grain slip activity in plastically deformed Zr determined by X-ray micro-diffraction line profile analysis. *Acta Materialia* **55** (2007) 1117–1127.

- [37] Hendricks, S. B.; Jefferson, M. E.; Schultz, J. F.: XXII. The transition temperatures of cobalt and of nickel, some observations on the oxides of nickel. *Z. Kristallogr.* **73** (1930) 376–380.
- [38] Landau, L.: The scattering of X-rays by crystals with variable lamellar structure. *Phys. Z. SowjUn.* **12** (1937) 579–585.
- [39] Lifschitz, M.: On the theory of scattering of X-rays by crystals of variable structure. *Phys. Z. SowjUn.* **12** (1937) 623–643.
- [40] Hendricks, S.; Teller, E.: X-ray interference in partially ordered layer lattices. *J. Chem. Phys.* **10** (1942) 147–167.
- [41] Jagodzinski, H.: Eindimensionale Fehlordnung in Kristallen und ihr Einfluss auf die Röntgeninterferenzen. II. Berechnung der fehlgeordneten dichtesten Kugelpackungen mit Wechselwirkungen der Reichweite 3. *Acta Cryst.* **2** (1949) 208–214.
- [42] Treacy, M. M. J.; Newsam, J. M.; Deem, M. W.: A general recursion method for calculating diffracted intensities from crystals containing planar faults. *Proc. Roy. Soc. London* **A433** (1991) 499–520.
- [43] Ustinov, A. I.: Defect and Microstructure Analysis by Diffraction (Eds. R. L. Snyder, J. Fiala, and H. J. Bunge) pp. 264–317. Oxford University Press, 1999.
- [44] Ustinov, A. I.; Olikhovska, L. O.; Budarina, N. M.; Bernard, F.: Diffraction analysis of the microstructure of materials (Eds. E. J. Mittemeijer, P. Scardi) p. 309. Springer-Verlag, Berlin, Heidelberg, 2004.
- [45] Scardi, P.; Leoni, M.: Fourier modelling of the anisotropic line broadening of X-ray diffraction profiles due to line and plane lattice defects. *J. Appl. Cryst.* **32** (1999) 671–682.
- [46] Estevez-Rams, E.; Penton-Madrugal, A.; Lora-Serrano, R.; Martinez-Garcia, J.: Direct determination of microstructural parameters from the X-ray diffraction profile of a crystal with stacking faults. *J. Appl. Cryst.* **34** (2001) 730–736.
- [47] Estevez-Rams, E.; Lora-Serrano, R.; Penton-Madrugal, A.; Fuess, H.: Quantitative analysis of planar faulting. *Acta Cryst.* **A58** (Supplement) (2002) C233.
- [48] Estevez-Rams, E.; Leoni, M.; Scardi, P.; Aragon-Fernandez, B.; Fuess, H.: On the powder diffraction pattern of crystals with stacking faults. *Philosophical Magazine.* **83** (2003) 4045–4057.
- [49] Leoni, M.; Gualtieri, A. F.; Roveri, N.: Simultaneous refinement of structure and microstructure of layered materials. *J. Appl. Cryst.* **37** (2004) 166–173.
- [50] Kuznetsov, A.; Dmitriev, V.; Langenhorst, F.; Estevez-Rams, E.; Dubrovinskaya, L.: Stacking Faults and Internal Strains in DHCP Phase of La. *Acta Cryst.* **A61** (2005) C451
- [51] Balogh, L.; Ribárik G.; Ungár, T.: Stacking Faults and Twin Boundaries in fcc Crystals Determined by X-ray Diffraction Profile Analysis. *J. Appl. Phys.* **100** (2006) 023512.
- [52] Ungár, T.; Mughrabi, H.; Rönnpagel D.; Wilkens, M.: X-ray line-broadening study of the dislocation cell structure in deformed [001]-orientated copper single crystals. *Acta Met.* **32** (1984) 333–342.
- [53] Mughrabi, H.; Ungár, T.; Kienle W.; Wilkens, M.: Long range internal stresses and asymmetric X-ray line broadening in tensile-deformed [001]-orientated copper single crystals. *Phil. Mag.* **A53** (1986) 793–813.
- [54] Noyan, I. C.; Cohen, J. B.: Residual stress: measurement by diffraction and interpretation. Spinger-Verlag, New York, 1987.
- [55] Lahman, D.; Field, R.; Darolia R.; Fraser, H.: Investigation of techniques for measuring lattice mismatch in a rhenium containing nickel base superalloy. *Acta metall.* **36** (1988) 1309–1320.
- [56] Kuhn, H. A.; Biermann, H.; Ungár, T.; Mughrabi, H.: X-ray study of creep-deformation induced changes of the lattice mismatch in the  $\gamma'$ -hardened monocrystalline nickel-base superalloy SRR 99. *Acta Met. Mater.* **39** (1991) 2783–2794.
- [57] Mughrabi, H.; Biermann, H.; Ungár, T.: Creep-induced local lattice parameter changes in a monocrystalline Nickel-base superalloy. *Journal of Materials Engineering and Performance* **2** (1993) 557–564.
- [58] Ungár, T.; Biermann, H.; von Grossmann, B.: Synchrotron microbeam diffraction study of the microstructure and the chemical composition in a monocrystalline Ni-base turbine blade after a thermo mechanical mission test. *Structural Chemistry* **14** (2003) 49–56.
- [59] Leineweber, A.; Mittemeijer, E. J.: Anisotropic microstrain broadening due to compositional inhomogeneities and its parametrisation. *Z. Kristallogr. Suppl.* **23** (2006) 117–122, Part 1.
- [60] Wilson, A. J. C.; Zsoldos, L.: The Reflexion of X-Rays from the ‘Anti-Phase Nuclei’ of AuCu<sub>3</sub>. II. *Proc Roy Soc London* **A290** (1966) 508–514.
- [61] Scardi, P.; Leoni, M.: Diffraction whole-pattern modelling study of anti-phase domains in Cu<sub>3</sub>Au. *Acta Materialia* **53** (2005) 5229–5239.
- [62] Schafner, E.; Steiner, G.; Korznikova, E.; Kerber M.; Zehetbauer, M. J.: Lattice defect investigation of ECAP-Cu by means of X-ray line profile analysis, calorimetry and electrical resistometry. *Mater. Sci. Eng.* **A410–411** (2005) 169–173.
- [63] Cervellino, A.; Giannini, C.; Guagliardi, A.; Ladisa, M.: Nanoparticle size distribution estimation by a full-pattern powder diffraction analysis *Phys. Rev.* **B72** (2005) 035412.
- [64] Ribárik, G.; Audebrand, N.; Palancher, H.; Ungár, T.; Louër, D.: Dislocations and crystallite size distributions in ball-milled nanocrystalline fluorides MF<sub>2</sub> (M = Ca, Sr, Ba, Cd) determined by X-ray diffraction-line-profile analysis, *J. Appl. Cryst.* **38** (2005) 912–926.
- [65] Palosz, B.; Stelmakh, S.; Grzanka, E.; Gierlotka, S.; Palosz, W.: Application of the apparent lattice parameter to determination of the core-shell structure of nanocrystals. *Z. Kristallogr.* **222** (2007) 580–594.
- [66] Ungár, T.; Gubicza, J.: Nanocrystalline Materials Studied by Powder Diffraction Line Profile Analysis. *Z. Kristallogr.* **222** (2007) 114–128.
- [67] Bertaut, E. F.: Raies de Debye-Scherrer et repartition des dimensions des domaines de Bragg dans les poudres polycristallines. *Acta Cryst.* **3** (1950) 14–18.
- [68] Ungár, T.; Gubicza, J.; Ribárik, G.; Borbély, A.: Crystallite size distribution and dislocation structure determined by diffraction profile analysis: Principles and practical application to cubic and hexagonal crystals. *J. Appl. Cryst.* **34** (2001) 298–310.
- [69] Guinier, A.: X-ray Diffraction. Freeman, San Francisco, (1963).
- [70] Leoni, M.; Scardi, P.: Nanocrystalline domain size distributions from powder diffraction data. *J. Appl. Cryst.* **37** (2004) 629–634.
- [71] Langford, J. I.; Boulton, A.; Auffrédic, J. P.; Louër, D.: The use of pattern decomposition to study the combined X-ray diffraction effects of crystallite size and stacking-faults in ex-oxalate zinc-oxide. *J. Appl. Cryst.* **26** (1993) 22–33.
- [72] Louër, D.; Auffrédic, J. P.; Langford, J. I.; Ciosmak D.; Niepce, J. C.: A precise determination of the shape, size and distribution of size crystallites in zinc-oxide by X-ray line broadening analysis. *J. Appl. Cryst.* **16** (1983) 183–191.
- [73] Williamson, G. K.; Hall, W. H.: X-ray Line Broadening from Filed Al and W. *Acta metall.* **1** (1953) 22–31.
- [74] Stokes, A. R.; Wilson, A. J. C.: A method of calculating the integral breadths of Debye-Scherrer lines. *Proc. Camb. Phil. Soc.* **38** (1942) 313–322.
- [75] Kuzel Jr., R.; Klimanek, P.: X-ray diffraction line broadening due to dislocations in non-cubic materials. 2. The case of elastic-anisotropy applied to hexagonal crystals. *J. Appl. Cryst.* **21** (1988) 363–368.
- [76] Kuzel Jr., R.; Klimanek, P.: X-ray diffraction line broadening due to dislocations in non-cubic materials. 3. Experimental results for plastically deformed zirconium. *J. Appl. Cryst.* **22** (1989) 299–307.
- [77] Ungár, T.; Borbély, A.: The effect of dislocation contrast on X-ray line broadening: a new approach to line profile analysis. *Appl. Phys. Lett.* **69** (1996) 3173–3175.
- [78] Révész, Á.; Ungár, T.; Borbély A.; Lendvai, J.: Dislocations and grain size in ball-milled iron powder. *Nanostr. Mater.* **7** (1996) 779–788.
- [79] Hinds, W. C.: Aerosol Technology: Properties, Behavior and Measurement of Airborne Particles, New York: Wiley, 1982.
- [80] Scardi, P.; Leoni, M.; Delhez, R.: Line broadening analysis using integral breadth methods: a critical review. *J. Appl. Cryst.* **37** (2004) 381–390.
- [81] Ungár, T.; Gubicza, J.; Tichy, G.; Pantea C.; Zerda, T. W.: Size and shape of crystallites and internal stresses in carbon blacks. *Composites Part A: Applied Science and manufacturing* **36** (2005) 431–436.
- [82] Pantea, C.; Gubicza, J.; Ungár, T.; Voronin, G.; Zerda, T. W.: Dislocation density and graphitization of diamond crystals. *Phys. Rev.* **B66** (2002) art. no. 094106.

- [83] Scardi, P.; Dong, Y.; Leoni, M.: Line profile analysis in Rietveld method and Whole Powder Pattern Fitting. *Mater. Sci. Forum* **378–381** (2001) 132–139.
- [84] Ribárik, G.; Ungár, T.; Gubicza, J.: MWP-fit: A program for multiple whole-profile fitting of diffraction peak profiles by ab initio theoretical functions. *J. Appl. Cryst.* **34** (2001) 669–676.
- [85] Scardi, P.; Leoni, M.: Whole powder pattern modelling. *Acta Cryst.* **A58** (2002) 190–200.
- [86] Velterop, L.; Delhez, R.; deKeijser, T. H.; Mittemeijer E. J.; Reefman, D.: X-ray diffraction analysis of stacking and twin faults in F.C.C metals: a revision and allowance for texture and non-uniform fault probabilities. *J. Appl. Crystallogr.* **33** (2000) 296–306.
- [87] Dragomir, I. C.; Ungar, T.: Contrast factors of dislocations in the hexagonal crystal system. *J. Appl. Cryst.* **35** (2002) 556–564.
- [88] Ungár, T.; Glavicic, M. G.; Balogh, L.; Nyilas, K.; Salem, A. A.; Ribárik G.; Semiatin, S. L.: *Mater. Sci. Eng. A*, submitted.
- [89] Balogh, L.; Ribárik, G.; Ungár, T.: in preparation.
- [90] Ungár, T.: Micro structural parameters from X-ray diffraction peak broadening. *Scripta Mater.* **51** (2004) 777–781.
- [91] Zhilyaev, A. P.; Gubicza, J.; Nurislamova, G.; Révész, Á.; Suriñach, S.; Baró, M. D.; Ungár, T.: Microstructural Characterization of Ultrafine-Grained Nickel. *phys. stat. sol. (a)* **198** (2003) 263–271.
- [92] Chinh, N. Q.; Gubicza, J.; Langdon, T. G.: Face-centered cubic metals and alloys processed by Equal-Channel Angular Pressing. *J. Mater. Sci.* **42** (2007) 1594–1605.
- [93] Gubicza, J.; Chinh, N. Q.; Krállics, Gy.; Schiller, I.; Ungár, T.: Microstructure of ultrafine-grained fcc metals produced by severe plastic deformation. *Curr. Appl. Phys.* **6** (2006) 194–199.
- [94] Valiev, R. Z.; Islamgaliev, R. K.; Alexandrov, I. V.: Bulk nanostructured materials from severe plastic deformation. *Progr. Mater. Sci.* **45** (2000) 103–189.
- [95] Gubicza, J.; Chinh, N. Q.; Horita, Z.; Langdon, T. G.: Effect of Mg addition on microstructure and mechanical properties of aluminum. *Mater. Sci. Eng.* **A387–389** (2004) 55–59.
- [96] Zhu, Y. T.; Huang, J. Y.; Gubicza, J.; Ungár, T.; Wang, Y. M.; Ma, E.; Valiev, R. Z.: Nanostructures in Ti Processed by Severe Plastic Deformation. *J. Mat. Res.* **18** (2003) 1908–1917.
- [97] Kumar, K. S.; Suresh, S.; Chisholm, M. F.; Horton, J. A.; Wang, P.: Deformation of electrodeposited nanocrystalline nickel. *Acta Materialia* **51** (2003) 387–405
- [98] Swygenhoven, H.; Farkas, D.; Caro, A.: Grain-boundary structures in polycrystalline metals at the nanoscale. *Phys. Rev.* **B62** (2000) 831–838.
- [99] Swygenhoven, S. H.; Derlet, P. M.; Hasnaoui, A.: Atomistic Modeling of Strength of Nanocrystalline Metals. *Advanced Engineering Materials* **5** (2003) 345–350.
- [100] Schiøtz, J.; DiTolla, F. D.; Jacobsen, K. W.: Softening of nanocrystalline metals at very small grain sizes. *Nature* **391** (1998) 561–563.
- [101] Schiøtz, J.; Vegge, T.; DiTolla, F. D.; Jacobsen, K. W.: Atomic-scale simulations of the mechanical deformation of nanocrystalline metals. *Phys. Rev.* **B60** (1999) 11971–11983.
- [102] Yoo, M. H.: Slip, twinning and fracture in hexagonal close-packed metals. *Metall. Trans.* **A12** (1981) 409–418.
- [103] Ungár, T.; Tichy, G.; Sanders, P. G.; Weertman, J. R.: Dislocations in Submicron Grain Size and Nanocrystalline Copper. *Mater. Res. Soc. Symp. Proc.* **634** (2001) B1.7.1–6.
- [104] Weertman, J. R.; Sanders, P. G.: Plastic Deformation of Nanocrystalline Metals. *Solid State Phenomena* **35–36** (1994) 249–262.
- [105] Sanders, P. G.: Ph.D. thesis. Northwestern University, 1996.
- [106] Sanders, P. G.; Fougere, G. E.; Thompson, L. J.; Eastman, J. A.; Weertman, J. R.: Improvements in the synthesis and compaction of nanocrystalline materials. *Nanostruct. Mater.* **8** (1997) 243–252.
- [107] Valiev, R. Z.; Kozlov, E. V.; Ivanov, Yu.; F. Lian, J.; Nazarov, A. A.; Baudalet, B.: Deformation behavior of ultra-fine-grained copper. *Acta Metall. Mater.* **42** (1994) 2467–2475.
- [108] Baik, S. C.; Estrin, Y.; Kim, H. S.; Jeong, H. T.; Hellmig, R. J.: Calculation of deformation behavior and texture evolution during equal channel angular pressing of IF steel using dislocation based modeling of strain hardening. *Mater. Sci. Forum* **408–412** (2002) 697–702.
- [109] Zhu, Y. T.; Liao, X. Z.; Srinivasan, S. G.; Lavernia, E. J.: Nucleation of deformation twins in nanocrystalline face-centered-cubic metals processed by severe plastic deformation. *J. Appl. Phys.* **98** (2005) 034319.
- [110] Zhao, Y. H.; Zhu, Y. T.; Liao, X. Z.; Horita, Z.; Langdon, T. G.: Tailoring stacking fault energy for high ductility and high strength in ultrafine grained Cu and its alloy. *Appl. Phys. Lett.* **89** (2006) 121906.
- [111] Louër, D.; Auffredic, J. P.; Langford, J. I.; Ciosmak, D.; Niepce, J. C.: Thermodynamic study of the thermal decomposition of zinc hydroxinitrates. *J. Appl. Cryst.* **183** (1983) 16–23.
- [112] Lin, J. D.; Duh, J. G.: The use of X-ray line profile analysis in the tetragonal to monoclinic phase transformation of ball milled, as-sintered and thermally aged zirconia powders. *J. Mat. Sci.* **32** (1997) 4901–4908.
- [113] Palosz, B.; Grzanka, E.; Pantea, C.; Zerda, T. W Wang.; Gubicza, J.; Ungár, T.: Microstructure of nanocrystalline diamond powders studied by powder diffractometry. *J. Appl. Phys.* **97** (2005) 064316.
- [114] Gubicza, J.; Nauyoks, S.; Balogh, L.; Zerda, T. W.; Ungár, T.: Influence of sintering temperature and pressure on crystallite size and lattice defect structure in nanocrystalline SiC. *J. Mater. Res.* **22** (2007) 1314–1321.
- [115] Wilhelm, H.; Paris, A.; Schafner, E.; Bernstorff, S.; Bonarski, J.; Ungar, T.; Zehetbauer, M. J.: Evidence of dislocations in melt-crystallised and plastically deformed polypropylene. *Materials Science and Engineering* **A387–389** (2004) 1018–1022.
- [116] Lin, L.; Argon, A. S.: Structure and plastic deformation of polyethylene. *J. Mater. Sci.* **29** (1994) 294–323.